ARTICLE Open Access

Retinal thermal deformations measured with phase-sensitive optical coherence tomography in vivo

Yueming Zhuo[1,2]✉, Mohajeet Bhuckory[2,3], Huakun Li[4], Junya Hattori[5], Davis Pham-Howard[2,3], David Veysset[6], Tong Ling[4,7,8,9] and Daniel Palanker[2,3]✉

Abstracts

Controlling the tissue temperature rise during retinal laser therapy is essential for predictable outcomes, especially at non-damaging settings. We demonstrate a method for determining the temperature rise in the retina using phase-sensitive optical coherence tomography (pOCT) in vivo. Measurements based on the thermally induced optical path length changes (ΔOPL) in the retina during a 10-ms laser pulse allow detection of the temperature rise with a precision less than 1 °C, which is sufficient for calibration of the laser power for patient-specific non-damaging therapy. We observed a significant difference in confinement of the retinal deformations between the normal and the degenerate retina: in wild-type rats, thermal deformations are localized between the retinal pigment epithelium (RPE) and the photoreceptors' inner segments (IS), as opposed to a deep penetration of the deformations into the inner retinal layers in the degenerate retina. This implies the presence of a structural component within healthy photoreceptors that dampens the tissue expansion induced by the laser heating of the RPE and pigmented choroid. We hypothesize that the thin and soft cilium connecting the inner and outer segments (IS, OS) of photoreceptors may absorb the deformations of the OS and thereby preclude the tissue expansion further inward. Striking difference in the confinement of the retinal deformations induced by a laser pulse in healthy and degenerate retina may be used as a biomechanical diagnostic tool for the characterization of photoreceptors degeneration.

Introduction

Precise control of the temperature rise in tissue during laser therapy is essential for predictable and reproducible outcomes. The energy absorption and associated temperature rise depend on the irradiation parameters (wavelength, power, duration, spot size, etc.) and on tissue properties (light scattering and absorption, thermal conductivity, heat capacity, etc.). In retinal laser treatments[1], light delivered to the retina is absorbed primarily by melanin, which is highly concentrated in the retinal pigmented epithelium (RPE) and pigmented choroid[2,3]. Melanin concentration varies significantly between individuals, as well as across the retina within the same subject, up to a factor of four[4]. Moreover, the transmittance of the transparent ocular tissues (cornea, lens, vitreous, and inner retina) decreases with age and might be affected by diseases, hence reducing the temperature rise in the retina[5,6]. If such variations are not accounted for, they can result in over- or under-treatment of the retina.

The dosimetry of hyperthermia can be quantified assuming that cells respond to a decrease in concentration of biomolecules due to thermal denaturation. Assuming first-order reaction kinetics[7], Arrhenius equation describes the reaction rate:

$$\frac{dc}{dt} = -A \cdot c \cdot \exp\left(-\frac{E^*}{k \cdot T(t)}\right) \quad (1)$$

Correspondence: Yueming Zhuo (zym9426@stanford.edu) or Daniel Palanker (palanker@stanford.edu)
[1]Department of Electrical Engineering, Stanford University, Stanford, CA 94305, USA
[2]Hansen Experimental Physics Laboratory, Stanford University, Stanford, CA 94305, USA
Full list of author information is available at the end of the article
These authors contributed equally: Mohajeet Bhuckory, Huakun Li

© The Author(s) 2025
Open Access This article is licensed under a Creative Commons Attribution 4.0 International License, which permits use, sharing, adaptation, distribution and reproduction in any medium or format, as long as you give appropriate credit to the original author(s) and the source, provide a link to the Creative Commons licence, and indicate if changes were made. The images or other third party material in this article are included in the article's Creative Commons licence, unless indicated otherwise in a credit line to the material. If material is not included in the article's Creative Commons licence and your intended use is not permitted by statutory regulation or exceeds the permitted use, you will need to obtain permission directly from the copyright holder. To view a copy of this licence, visit http://creativecommons.org/licenses/by/4.0/.

where c is the concentration of a critical biomolecule, E^* is the reaction activation energy, k—Boltzmann constant and T—absolute temperature. Integration of the reaction rate over time yields the total fraction of the denatured biomolecules during hyperthermia, compared to its initial concentration c_0:

$$\ln\frac{c(\tau)}{c_0} = -A\int_0^{\tau} e^{-\frac{E^*}{kT(t)}}dt = -\Omega(\tau) \quad (2)$$

where A is the reaction rate constant (s^{-1}), and τ is the duration of hyperthermia. The rate constant A is normalized to $\Omega = 1$ to define the threshold of tissue damage. It has been established that retinal response to hyperthermia becomes noticeable when $\Omega > 0.1$, thereby defining the therapeutic window of non-damaging thermal therapy to $0.1 < \Omega < 1$[8–10].

In current clinical practice, retinal laser damage threshold is often determined by subjective evaluation of the test lesions in the periphery of the retina by a physician[11], which is prone to subjective judgment. Unlike surface heating of the tissue, where mid-infrared (3–10 μm) radiation propagating through the air to infrared camera can help assess the surface temperature, strong absorption of mid-infrared radiation by water precludes such measurements inside the eye. Recently, a photoacoustic system was introduced, which uses a pulsed laser to induce thermoelastic expansion of melanosomes and measures the pressure transients to determine the temperature and optimize the laser power or exposure duration for a desired treatment outcome[12]. This technique was not yet accepted in clinical practice due to the need for a more expensive and complex laser system and photoacoustic detection.

Mapping of the retinal temperature rise in response to low-power laser pulses by phase-sensitive optical coherence tomography (pOCT) prior to laser treatment has been proposed as a non-invasive alternative[13–15]. In the future, when OCT machines will be upgraded to phase-sensitive detection, such mapping could be performed by the same tool as the structural OCT, and laser settings could be adjusted automatically during treatment according to these maps using computer-guided systems, such as PASCAL or Navilas[16,17]. Optical path length changes (ΔOPL) in OCT provide high sensitivity in detecting minute thermal responses in tissue, and have been shown to correlate with temperature measurements[18,19]. In our previous work, we have demonstrated how pOCT allows for precise detection of laser-induced thermal transients ex-vivo[20]. Tissue parameters and temperature profiles were extracted using a thermo-mechanical model[21], which was subsequently validated by a temperature-sensitive fluorescence imaging[20].

In this study, we demonstrate that a similar approach can be reproduced in-vivo, utilizing a subpixel registration algorithm for compensating the bulk tissue motion due to heartbeat, breathing cycle, and eye movements. Our results reveal an unexpected difference in the thermal deformation patterns between normal and degenerate retina: the OPL changes in healthy retina are confined within the photoreceptor outer segments (OS), as opposed to a much deeper penetration of the tissue expansion in the degenerate retina. These findings indicate the presence of a soft structural element between the photoreceptors' OS and inner segments (IS), which we hypothesize to be the interconnecting cilium, that dampens the thermal expansion of the OS driven by laser heating of the underlying pigmented layers: RPE and choroid. We tested the validity of this hypothesis by thermo-mechanical modeling. This surprising phenomenon may provide diagnostic insight in evaluating the health of photoreceptors.

Results

Measuring the thermally induced OPL change with pOCT

Animal preparations and the retinal heating experiments were conducted under room light conditions. Two strands of pigmented rats have been used: wild-type Long Evans (LE) rats and Royal College of Surgeons (RCS) rats having retinal degeneration. To prevent optoretinographic (ORG) responses[22], the wild-type (WT) rat retinas were fully bleached using a full-field illumination from a green LED (CW, 50 μW, centered at 565 nm, illumination area about 6 mm^2, bleached for 3 min). RCS rats exhibit photoreceptor degeneration due to RPE's inability to phagocytose the rod OS[23], and their light-insensitive retinas were used to validate that thermal deformations are not induced by ORG responses. Animals were imaged by a custom-built high-speed line-scan spectral-domain optical coherence tomography (LS-SD-OCT) system (see *Materials and Methods*). Retinal cross-sectional scans were captured at 10 kHz frame rate. The heating laser beam at 532 nm wavelength was aligned at the center of the imaging line field (see Fig. S2) and was applied for 10 ms at 10.8 mW of power measured in front of the eye. To minimize motion caused by heartbeat and breathing, rat's head was stabilized using a custom-built stage equipped with a bite bar and ear bars.

An averaged B-scan of a 6-month-old WT rat is shown in Fig. 1a. The labeled IS/OS line is commonly attributed to the ellipsoid zone (EZ) of the IS, which is rich in mitochondria[24,25]. The connecting cilium, a narrow bridge linking the IS and OS of photoreceptors, is also suggested to be part of the hyperreflective IS/OS band[26]. This structure is crucial for the transport of proteins and other molecules necessary for the function and maintenance of the photoreceptor OS[27]. The thick hyperreflective band

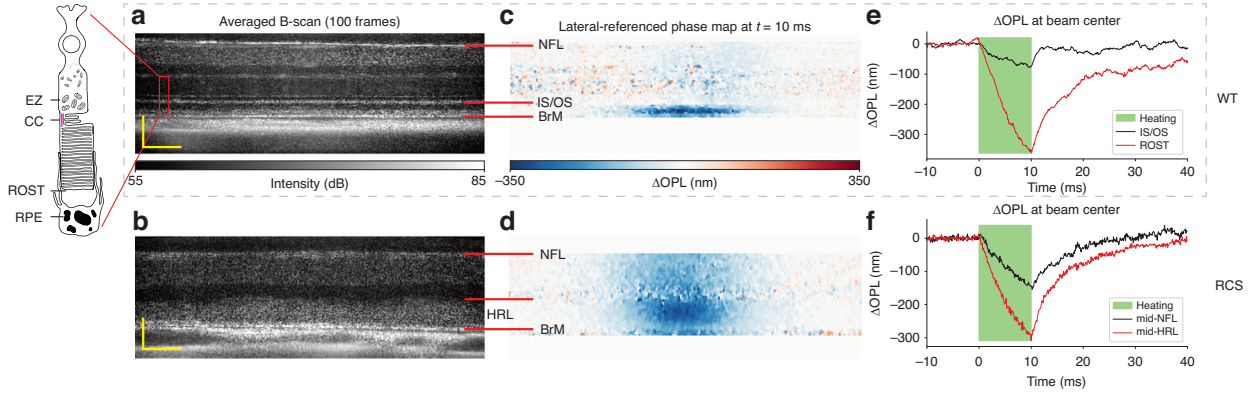

Fig. 1 Phase-sensitive OCT imaging of retinal deformations. a Averaged B-scan of a 6-month-old wild-type (WT) rat retina. SNR at BrM: 30 dB. Scale bar: axial—90 µm; lateral—50 µm. **b** Averaged B-scan of a 6-month-old RCS rat retina. SNR at RPE: 30 dB. Scale bar: axial—70 µm; lateral—50 µm. Labels on the photoreceptor diagram and B-scans: NFL nerve fiber layer, IS/OS inner segment and outer segment, BrM Bruch's membrane, EZ ellipsoid zone, CC connecting cilium, ROST rod outer segment tip, HRL hyperreflective layer, RPE retinal pigment epithelium. **c**, **d** Laterally referenced phase maps for WT and RCS rats at $t = 10$ ms. **e**, **f** OPL changes over time at beam center for WT and RCS rats

between the IS/OS junction and the Bruch's membrane (BrM) is composed of the rod OS and RPE, including the RPE microvilli interdigitating with the rod outer segment tips (ROST)[28]. As shown in the averaged B-scan of the same age RCS rat retina (Fig. 1b), the degenerated rod OS have formed a hyperreflective layer (HRL) above the RPE. The imaging quality of the WT retina is generally better than RCS retina due to healthier eye optics.

To correct for bulk tissue motion between repeated B-scans, a custom image registration algorithm, called phase-restoring subpixel image registration (PRESIR) was employed[29]. To map the tissue deformations induced by heating, we calculated pixelwise phase changes between subsequent frames and the first frame. To eliminate the residual phase changes induced by the rigid motion of the retina, such as eye rotation, edges of the OCT B-scan were used as the lateral reference region (see *Materials and Methods* and *Supplementary Information*, Fig. S3). Doing so, we obtained the tissue dynamics with respect to the edges of the OCT B-scan (Fig. 1c, d).

As expected, during the laser heating (Fig. 1e, f), thermal expansion of tissue leads to a negative change in OPL from the combined effects of tissue moving anteriorly and decrease in refractive index as the temperature rises. After the laser pulse, heat diffuses away, and tissue cools down, gradually returning to its initial state.

Surprisingly, significant difference was observed between the ΔOPL maps of RCS and WT retinas. In RCS retina, the OPL change decreases from its maximum value in the HRL to about half of it in the NFL (Fig. 1d, f, Movie S1). However, in WT retina, the OPL changes of a similar magnitude are confined between BrM and IS/OS junction, with negligible changes above it (Fig. 1c, e, Movie S2). Figure S4 in Supplementary Information demonstrates reproducibility of the signal patterns between different WT rats. The OPL changes in the inner retina, photoreceptor outer segment layer (HRL in the case of RCS group), and in the BrM were extracted and compared between two groups (see statistical plot in Fig. S5). This pronounced localization of the retinal deformation within the outer segment area implies that the WT retina has a particularly soft structural element below the inner segment that effectively absorbs the thermal strain originating from the heating of RPE and pigmented choroid layers below.

Thermomechanical modeling of the retina

Thermally induced OPL changes can be attributed to tissue expansion and to changes in refractive index. To extract the tissue temperature, a model of ΔOPL should be computed, based on the temperature fields and the vertical displacements of retinal layers, which are both solutions to a thermo-mechanical problem with coupled equations of elasticity and heat diffusion. Here, we briefly describe the model setup, following[20,21].

The retina is modeled as an axisymmetric multi-layered medium composed of isotropic elastic solid layers. Thermal stress arises from the heat generated by the laser energy absorbed in the RPE and in pigmented choroid. We define the optical transmittance through the eye to the RPE layer as η, the spatio-temporal profile of the heat flux at the RPE layer along the depth z can be written based on the Beer-Lambert law:

$$q_{\mathrm{RPE}}(r,z,t) = \frac{\eta P_{in}}{\pi R^2}\Phi(r,t)\mu_a e^{-(\mu_a+\mu_s')z} \quad (3)$$

where P_{in} denotes the input power measured in front of the eye, R is the heating spot radius, $\Phi(r,t)$ is the spatiotemporal profile of the laser pulse with r and t denoting radial and temporal components respectively, μ_a is the absorption coefficient, and $\mu_s' = \mu_s(1-g)$ is the reduced scattering coefficient with μ_s being the scattering coefficient and g the anisotropy factor. The local heat flux at the pigmented choroid layer can be written in a similar fashion, taking into account that the incident laser power is attenuated by the RPE layer above.

For modeling purposes, all volumetric heat sources were discretized into surface heat sources that are sufficiently close to each other, so the characteristic heat diffusion time across them is much shorter than the 10-ms laser pulse duration[20]. For instance, heat diffusion time across 1-μm thick RPE apical layer is about 2.5 μs. Magnitude of the surface heat source at the top of the RPE apical layer was set to be equal to the total heat deposited in it (see Supplementary Information). The 20-μm thick pigmented choroid layer was discretized into five 4-μm thick layers, and a surface heat source was applied at the top of each layer.

In cylindrical coordinates, assuming quasi-static conditions, the governing partial differential equations of motion in equilibrium for an elastic layer are:

$$\frac{\partial \sigma_r}{\partial r} + \frac{\partial \tau_{rz}}{\partial z} + \frac{\sigma_r - \sigma_\theta}{r} = 0 \tag{4}$$

$$\frac{\partial \tau_{rz}}{\partial r} + \frac{\partial \sigma_z}{\partial z} + \frac{\tau_{rz}}{r} = 0 \tag{5}$$

where σ_r, σ_θ, and σ_z are the normal stress components, τ_{rz} is the shear stress in the r-z plane. The isotropic stress-strain constitutive relations including the thermal stress are:

$$\sigma_r + \beta\Theta = \lambda\epsilon_v + 2G\frac{\partial u_r}{\partial r} \tag{6}$$

$$\sigma_\theta + \beta\Theta = \lambda\epsilon_v + 2G\frac{u_r}{r} \tag{7}$$

$$\sigma_z + \beta\Theta = \lambda\epsilon_v + 2G\frac{\partial u_z}{\partial z} \tag{8}$$

$$\tau_{rz} = G\left(\frac{\partial u_r}{\partial z} + \frac{\partial u_z}{\partial r}\right) \tag{9}$$

where u denotes displacements, G is the shear modulus, λ is the Lame's first parameter, ϵ_v denote the volumetric strain, and Θ denotes the temperature rise. The thermo-mechanical coupling parameter β is linear to the thermal expansion coefficient α_{TE}, i.e.,

$$\beta = 2G\alpha_{\mathrm{TE}}\frac{1+\nu}{1-2\nu} \tag{10}$$

where ν is the Poisson's ratio. The heat transfer is described by the Fourier's heat conduction law:

$$\mathbf{q} = -\kappa\nabla\Theta \tag{11}$$

and the heat diffusion equation:

$$\frac{\partial\Theta}{\partial t} = \frac{\kappa}{\rho c_p}\nabla^2\Theta \tag{12}$$

where $\boldsymbol{q} = [q_r, q_z]^T$ is the heat flux vector, ∇ and ∇^2 denote gradient operator and Laplacian operator, respectively. κ is the thermal conductivity, ρ is the material density, and c_p is the material specific heat capacity. The heat flow in the z-direction can be computed by:

$$Q = \int_0^t q_z d\tau \tag{13}$$

All above equations are coupled to form the complete thermo-mechanical problem of a single layer.

The solution to the thermo-mechanical problem of a multi-layered medium with several absorptive layers is fully derived in the Supplementary Information. In brief, by transforming the above equations into the Hankel-Laplace (HL) domain, i.e., transforming from the primal domain (r,z,t) to HL domain (ξ,z,s), a stress vector $\mathbf{V}(\xi,z,s) = \left[\widetilde{\tau}_{rz}^{(1)}, \widetilde{\sigma}_z^{(0)}, \widetilde{Q}^{(0)}\right]^T$ is related to a state vector $\mathbf{\Lambda}(\xi,z,s) = \left[\widetilde{u}_r^{(1)}, \widetilde{u}_z^{(0)}, \widetilde{\Theta}^{(0)}\right]^T$ by a transfer matrix $\mathbf{K}(\xi,z,s)$ for a single elastic layer[30–33], i.e.,

$$\mathbf{V}(\xi,z,s) = \mathbf{K}(\xi,z,s)\mathbf{\Lambda}(\xi,z,s) \tag{14}$$

The superscript denotes the order of HL transform. Matrix equations at different depths can be arranged together for the multi-layered retina model (see Fig. S1). The state vector can be solved by simple matrix multiplication. The numerical inverse HL transform converts the solution back into the primal domain.

Retinal temperature derived from this analytical model depends on the assumed biomechanical properties. Various methods have been employed to measure mechanical properties of ocular tissues, including atomic force microscopy (AFM)[34,35] and optical coherence elastography (OCE)[36–38]. In this study, we use the biomechanical properties listed in Table S1 (see Supplementary Information), which are based on values reported in the literature and determined in our previous ex-vivo studies[20].

Temperature rise and displacement fields in the thermo-mechanical model of the WT retina are shown in Fig. 2. ΔOPL can be calculated at any point in space and time based on the temperature and tissue displacements

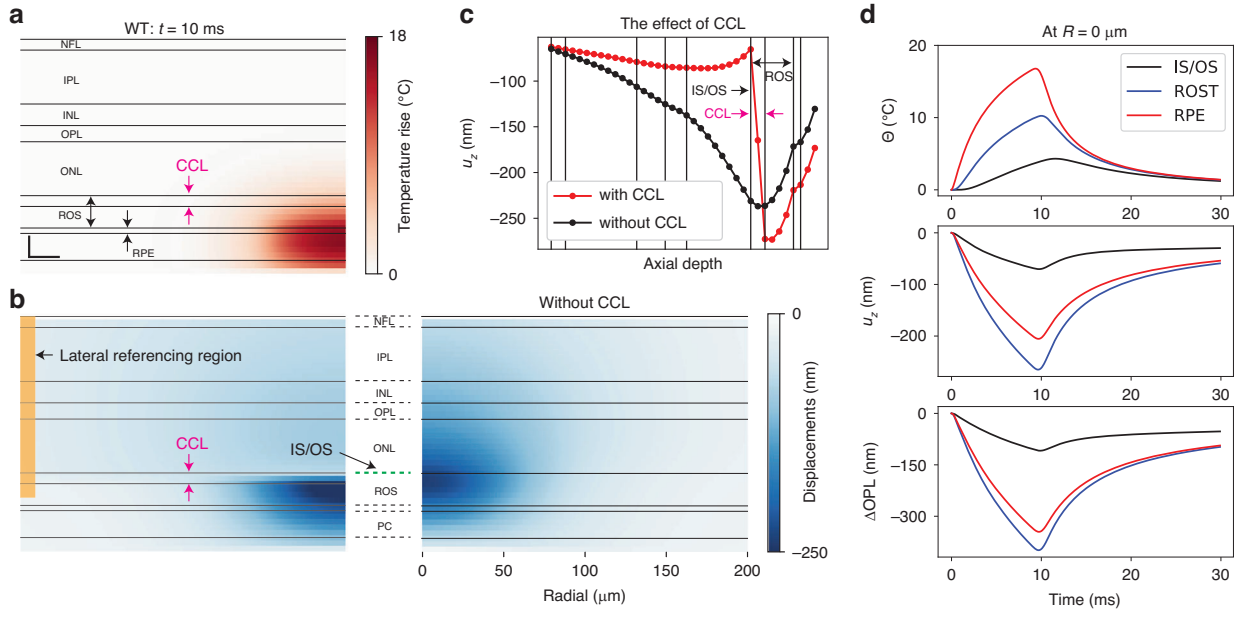

Fig. 2 Thermo-mechanical simulation results with parameters: $\eta = 50$ %, $C_\mu = 0.5$, $R = 45$ μm. a Simulated temperature map at $t = 10$ ms. Scale bar: axial—20 μm; lateral—20 μm. **b** Simulated displacement map at $t = 10$ ms with the CCL (left) and without it (right). To determine the reference OPL change similarly to the experimental phase processing (see *Materials and Methods*), the OPL changes within the lateral referencing region were averaged (yellow rectangle). **c** Tissue displacement profile showing the effect of the CCL layer. **d** Time course of displacements, temperature, and OPL change at the beam center for various layers. CCL connecting cilium layer

(Fig. 2d, *Materials and Methods*). To account for the strongly confined OPL change observed in Fig. 1c, we added a soft elastic layer, corresponding to the connecting cilium layer (CCL), between the IS/OS line and the rod OS. The connecting cilium (CC) is a thin, 0.3–0.5 μm wide, 1–2 μm long structure that forms the only physical connection between the IS and OS[27,39]. The vertical placement of this junction varies between cells, forming a thicker hyperreflective line in the OCT B-scan. Note that the temperature dynamics derived from the heat diffusion equations are the same with or without the CCL, hence the temperature fields (Fig. 2a) are identical for both cases, but the displacement field becomes drastically different (Fig. 2b, c).

Thickness and stiffness (Young's modulus) of this soft layer are strongly correlated to maintain the same level of mechanical damping. With its thickness assumed to be equal to that of IS/OS line (about 10 μm), to match the OPL change above the IS/OS line up to NFL to experimental values (Fig. 1c), we adjusted the Young's modulus to 20 Pa. Such a low Young's modulus was reported in some neuronal cells[40,41]. The thinner layer would have to be even softer to provide a similar extent of mechanical damping.

Fitting the model parameters

The model fitting parameters include the ocular optical transmittance, absorption coefficient (proportional to the local melanin concentration) and eye magnification, which affects the heating laser spot size. Denoting a scaling factor C_μ relative to the literature value of the absorption coefficient, i.e., $9.976 \times 10^3\ \mathrm{cm}^{-1}$ for RPE and $2.494 \times 10^3\ \mathrm{cm}^{-1}$ for the pigmented choroid layer[42], the list of the fitting parameters chosen for this study is: η, C_μ, and R. Note that, C_μ scales the absorption coefficient of both the RPE layer and the pigmented choroid layer. The tissue thermal expansion coefficient was taken from our previous work[20] and all other tissue properties were listed in Table S1. The initial heating laser radius is chosen based on the geometrical optics approximation of the rat eye[43]. The optimization objective is to minimize the squared Frobenius norm of the difference matrix between the experimental and model-derived ΔOPL data:

$$\min_{\eta, C_\mu, R} ||\Delta\mathrm{OPL}^{(\mathrm{exp})} - \Delta\mathrm{OPL}^{(\mathrm{sim})}||_{\mathrm{F}}^2 \tag{15}$$

where the subscript F denotes the Frobenius norm. The plane near the upper boundary of the ROST-RPE complex was extracted as the $\Delta\mathrm{OPL}^{(\mathrm{exp})}$ (shown as the blue line in Fig. 3a). The distance between the center of the IS/OS line and the selected plane was measured via the structural OCT image and set in the model such that the $\Delta\mathrm{OPL}^{(\mathrm{sim})}$ plane is the same distance away from the IS/OS line. Good agreement was obtained between the model and the experimental ΔOPL data both radially and temporally

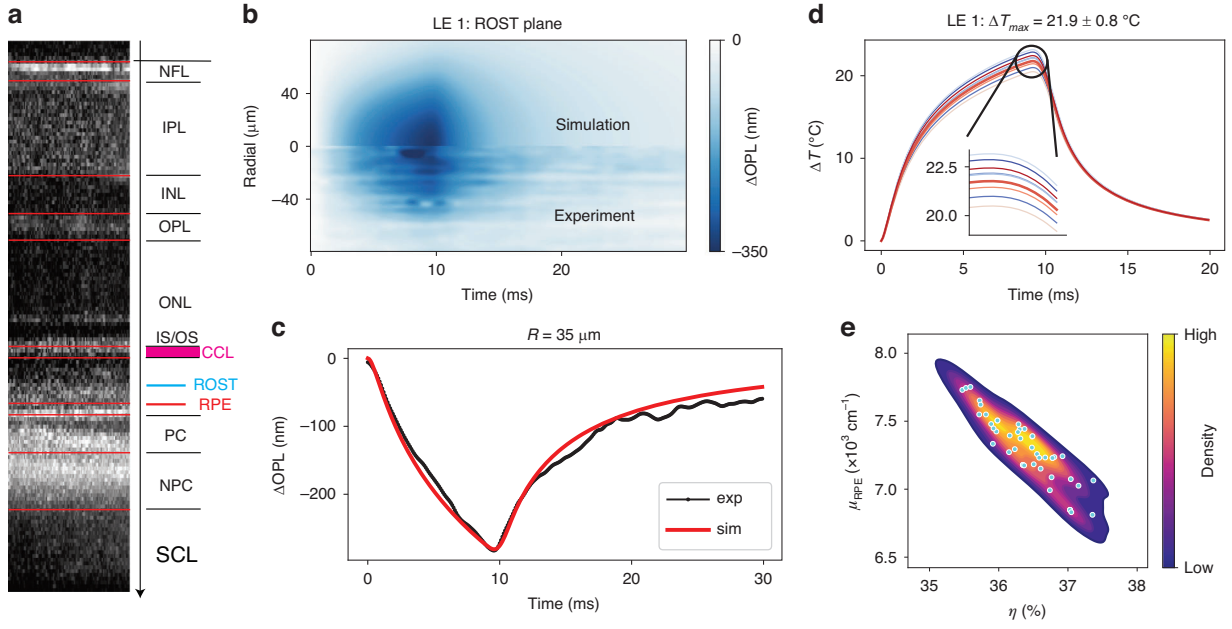

Fig. 3 Comparison between the model and experimental data. a WT retinal layer segmentation and denotation. The distance between the center of the IS/OS line and the blue plane where the OPL change was extracted was set the same in simulation and in experiment. **b** Spatio-temporal lateral-referenced ΔOPL map compared between the best-fit simulation (top) and experiment (bottom). **c** Example traces of ΔOPL and corresponding simulation, showing the heating and cooling dynamics. **d** Temperature time courses at the RPE computed with parameters collected from the last 10 iterations of the optimization process. **e** Contour plot showing the correlation between the absorption coefficient and optical transmittance via the bootstrapping analysis

Table 1 Parameter fitting and temperature estimation results

Rat #	P_{in}(mW)	$\eta^* \times C_\mu^*$	R^*(μm)	$\Delta T_{max}^{(RPE)}$(°C)	Arrh. integral
LE 1	10.8	0.308	33.0 (1.0)	21.9 (0.8)	0.199 (0.055)
LE 2	9.12	0.286	31.9 (0.9)	18.6 (0.7)	0.064 (0.015)
LE 3	9.12	0.300	32.4 (1.3)	18.0 (0.6)	0.050 (0.010)

Numbers in brackets are values of standard deviation

(Fig. 3b, c). The best-fit parameters and the peak temperature predictions are summarized in Table 1.

A forward pass thermo-mechanical simulation takes the initial fitting parameters with a prescribed laser dosage identical to the experimental laser settings and analytically solves displacement and temperature fields at any point in space and time. For parameter fitting optimization, the Nelder-Mead algorithm was utilized[44], which sometimes overshoots the parameters to avoid trapping in a local minimum (see Fig. S6A for an example convergence plot). To ensure robustness of the solution, 3 or 4 different initial points were tested, and the one which converges to the lowest objective function value was selected. The last 10 iterations of the optimization process near the minima were then used to compute parameter uncertainties and the peak temperature variations at the RPE layer (Fig. 3d). The derived temperature has uncertainty less than 1 °C, as listed in Table 1. Naturally, the optical transmittance and the absorption coefficient (Eq. (1)) are strongly coupled, with the product of the two (i.e., $\eta \times C_\mu$) representing the absorbed energy, as illustrated in Fig. 3e.

Using the model-predicted temperature profiles (Fig. 3d), it is possible to compute the associated Arrhenius integral and its uncertainty (Table 1). Heating of LE 1 retina was within the therapeutic window ($0.1<\Omega<1$), whereas the heating of LE 2–3 was performed at lower input power and resulted in sub-therapeutic Arrhenius integral $\Omega < 0.1$.

Temperature uncertainties can also be evaluated using a bootstrapping method[45,46], and the animal LE 1 was randomly selected for this analysis. By adding 50 sets of noise to the best-fit model-predicted ΔOPL data, the model was then re-fit to these noisy data to obtain the new best-fit parameters and associated peak temperature (see Supplementary Information). The 50 tuples of $(\eta, C_\mu)^\star$ obtained from fitting the bootstrapping data shows a highly eccentric elliptical shape in the contour plot (Fig. 3e) confirming that these parameters are strongly and negatively correlated. The resulting temperature courses had lower standard deviation of the peak temperature (see Fig. S6D) than values listed in Table 1.

Discussion

Laser therapy is applied to the retina in various disease conditions, aiming at preventing or diminishing the pathological effects of the disease on retinal structure and function. For example, in proliferative diabetic retinopathy, ablation of a significant fraction of photoreceptors in the peripheral retina reduces their metabolic load on diseased vasculature, preventing neovascularization and thereby saving the central vision[47]. In conditions of diabetic macular edema, central serous chorioretinopathy[9] and macular telangiectasia[48], the non-damaging retinal laser therapy helps reducing the intraretinal fluid accumulation by activation of the heat shock proteins, without damaging the photoreceptors or other retinal cells[10]. In all these conditions, photoreceptors are still in place, while in situations where photoreceptors are already lost, such as end-stage retinitis pigmentosa or geographic atrophy, lasers are not applied. Therefore, we expect that in clinically relevant conditions, retinal response to pulsed heating for laser calibration will include the localized deformation due to the dampening role of the highly compressible cilium, described above.

In addition to millisecond-range of laser pulses for heating and coagulation, micro- and nano-second pulses are used for more localized effects, such as selective destruction of cells in retinal pigment epithelium[49] and in trabecular meshwork[50]. We did not explore these pulse durations, but they may also benefit from calibration of the laser power using thermal deformations, as described in this study. Our experiments were conducted in rodents, where the use of anesthesia and the custom-built animal stage helped mitigate the bulk tissue motion. Under these well-controlled experimental conditions, our protocol using repeated cross-sectional scans proved sufficient for reliably extracting thermally induced tissue deformations. However, in future studies in human subjects, head movement is expected to introduce larger motion. The signal decorrelation caused by the out-of-plane motion could dramatically affect the phase stability. As in ORG studies in human subjects, we can extend the repeated B-scans to volumetric scans consisting of multiple densely sampled B-scans[22]. Although the volumetric scanning protocol will decrease the temporal resolution, it will help mitigate larger tissue movements.

In conclusion, measurement of the phase changes in OCT induced by sub-therapeutic heating of ocular tissues enables precise and safe temperature calibration for retinal laser therapy. In the future, when OCT machines will be upgraded to phase-sensitive detection, such mapping could be performed by the same tool as the structural OCT, and laser settings could be adjusted automatically during the treatment according to these maps using computer-guided scanning laser systems. Highly confined OPL change in WT retina, unlike the degenerate retina, suggests that cilium connecting the IS and OS in photoreceptors absorbs mechanical deformation induced by the thermal expansion. This feature might have a significant diagnostic value. Phase-sensitive OCT measurements of thermal deformations in various ocular tissues might also be useful for establishing more reliable safety regulations and the related safety standards.

Materials and methods

For detailed derivation of the analytical thermo-mechanical model see Supplementary Information.

Phase-sensitive OCT imaging

The high-speed line-scan spectral-domain OCT was assembled according to the optical layout shown in Fig. 4. The output of the supercontinuum laser (NKT FIR-9) was collimated (CL1, AC254-060-B) and filtered by two spectral filters (Semrock: FF01-776/LP-25, Thorlabs: FESH0900) yielding a bandwidth with a full-width at half-maximum (FWHM) of about 120 nm, centered at 840 nm.

A cylindrical lens (CYL1) focuses the beam along the x-axis forming a line along the y-axis at its focal plane. After optical conjugation of the afocal telescope L0-L1, the beam was split into reference and sample paths using a 30:70 (R:T) non-polarizing beamsplitter (Thorlabs, BSS11). In the sample arm, a one-dimensional galvo scanning (GS) mirror (8310 K Series Galvanometer, Cambridge Technology), which steers the beam in the y-direction, was aligned at the system pupil plane followed by two afocal telescopes, L2-L3 and L4-L5. The lens L5 and the animal stage were placed together on the Badal platform to adjust beam focus on the retina. In the reference arm, a cylindrical lens (CYL1R) re-collimated the elliptical beam into a circular beam followed by an afocal telescope (L1R-L2R). A prism pair (#43-649, Littrow Dispersion Prism, Edmund Optics) was used to empirically balance the dispersion mismatch between the two arms during the experiment. For the detection path, the image plane was anamorphically conjugated to the slit using two cylindrical lenses (CYL2 and CYL3) and L2. The back-scattered light was diffracted by a 600 l/mm grating (WP-600/840-35×45, Wasatch Photonics) and finally focused on to the detector of the high-speed camera (Phantom v641) with an image size of 768 × 512 pixels (spectral × spatial). Note that the scanning laser ophthalmoscope camera was aligned to be parfocal with the OCT camera and it was used to find a focal plane in the retina using Badal stage before the pOCT imaging.

The heating beam path was coupled with the OCT illumination path using a dichroic mirror (DCM, NFD01-532-25×36, Semrock) and was aligned to be coaxial with the OCT illumination. The heating beam source was a 532-nm diode-pumped solid-state laser (DPSS, 85-GHS-

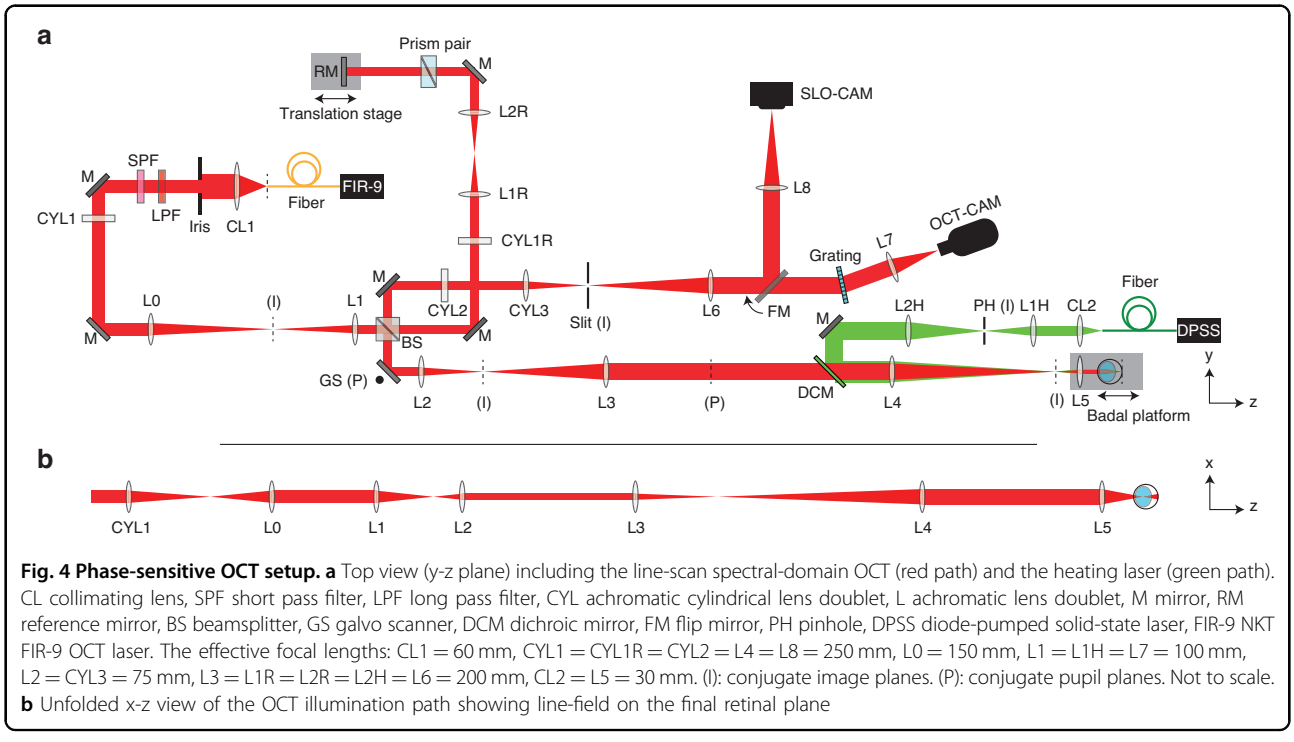

Fig. 4 Phase-sensitive OCT setup. a Top view (y-z plane) including the line-scan spectral-domain OCT (red path) and the heating laser (green path). CL collimating lens, SPF short pass filter, LPF long pass filter, CYL achromatic cylindrical lens doublet, L achromatic lens doublet, M mirror, RM reference mirror, BS beamsplitter, GS galvo scanner, DCM dichroic mirror, FM flip mirror, PH pinhole, DPSS diode-pumped solid-state laser, FIR-9 NKT FIR-9 OCT laser. The effective focal lengths: CL1 = 60 mm, CYL1 = CYL1R = CYL2 = L4 = L8 = 250 mm, L0 = 150 mm, L1 = L1H = L7 = 100 mm, L2 = CYL3 = 75 mm, L3 = L1R = L2R = L2H = L6 = 200 mm, CL2 = L5 = 30 mm. (I): conjugate image planes. (P): conjugate pupil planes. Not to scale. **b** Unfolded x-z view of the OCT illumination path showing line-field on the final retinal plane

305-042, Melles Griot) coupled into an optical fiber (NA = 0.22, diameter = 400 µm). The output of the fiber was collimated by CL2, and the tip of the fiber was conjugated to a pinhole with a diameter of 500 µm. The pinhole was demagnified and conjugated to OCT system image planes via the afocal telescope L2H-L4.

Animal preparation

All experimental procedures were approved by the Stanford Administrative Panel on Laboratory Animal Care and conducted in accordance with the institutional guidelines and conformed to the Statement for the Use of Animals in Ophthalmic and Vision research of the Association for Research in Vision and Ophthalmology (ARVO). LE rats (P60–P180) were used as a model of healthy retina and RCS rats were used as a model of outer retinal degeneration[23]. All RCS rats were aged until P120 to allow for complete photoreceptor degeneration, as validated by OCT (HRA2-Spectralis; Heidelberg Engineering, Heidelberg, Germany). Animal colonies were maintained at the Stanford Animal Facility in 12-h light/dark cycles with food and water ad libitum. Animals were anesthetized with a mixture of ketamine (75 mg/kg) and xylazine (5 mg/kg) injected intraperitoneally. The pupils were dilated with a mixture of 2.5% Phenylephrine Hydrochloride and 0.5% Tropicamide (Bausch & Lomb, Rochester, NY) ophthalmic solution and a zero-power contact lens (base curvature 3.00 mm, diameter 6.00 mm, optical power 0.00 D; Lakewood, CO 80226) was placed on the eye for imaging. Animals were placed on a custom animal stage and secured with a bite-bar and ear-bars to minimize movement.

Experimental ΔOPL data processing

We reconstructed complex-value OCT images from raw interferometric signals using k-linearity and discrete Fourier transform. To minimize decorrelation noise between repeated B-scans, we corrected bulk tissue motion with subpixel precision. Specifically, we estimated subpixel-level bulk displacements between first and the subsequent B-scans by locating the peak of unsampled cross-correlation maps[51]. Each B-scan was then registered to the first B-scan using the phase-restoring subpixel image registration algorithm, which shifts the complex-value OCT image over arbitrary displacements[29]. The registered B-scans were subsequently flattened along the BrM.

To further enhance phase stability, we self-referenced the phase changes to a region least affected by the stimulus - the edges of the B-scan and extracted the OPL change in tissue following the laser pulse relative to the edges[14,21].

To cancel out the arbitrary phase offset at each pixel, we first computed the multiplication of each B-scan with the complex conjugate of the first B-scan:

$$\widetilde{I}^{Tref}(x,z,t) = \widetilde{I}(x,z,t)\widetilde{I}^{*}(x,z,t_0) \tag{16}$$

where $\widetilde{I}(x,z,t)$ is the complex-valued OCT signal after image registration and flattening. $\widetilde{I}^{Tref}(x,z,t)$ is the

corresponding time referenced signal where x, z, and t denote the indices along the lateral, axial and temporal dimensions, respectively. t_0 denotes the time of the first frame, $*$ represents complex conjugate. The time referenced signal was further averaged across certain depth range to enhance the signal-to-noise ratio (SNR). In this study, we averaged the complex-valued signal from NFL to the BrM and then extracted the phase component:

$$\phi(x,t) = \measuredangle \sum_{z=z_1}^{z_2} \widetilde{I}^{Tref}(x,z,t) \tag{17}$$

where z_1 and z_2 are the axial indices of the upper boundary of NFL and the lower boundary BrM, respectively. Note that $\phi(x,t)$ consisted of both phase changes following laser heating and residual phase fluctuations due to bulk tissue motion. In ex vivo studies, a single reference point far from the heating beam was commonly selected to remove undesired phase fluctuations[14,20,21]. However, this strategy cannot be directly applied in vivo, as the rotational movement of the tissue resulted in varying phase along the lateral direction. Assuming the bulk motion, including both rotational and translational components, was rigid, the phase fluctuations should be linear along the lateral dimension[18]. Accordingly, phase signals $\phi(x_L,t)$ from a sequence of lateral positions x_L at the boundary of the OCT image (50 pixels on each side), which were least affected by the heating process, were selected to characterize the lateral phase shift. Specifically, $\phi(x,t)$ was first unwrapped along the lateral direction, resulting in $\phi^U(x,t)$. We then conducted a linear fitting between $\phi^U(x_L,t)$ and x_L to extract phase shift $\phi^{fit}(x,t) = p_0(t)x + p_1(t)$, where $p_0(t)$ and $p_1(t)$ are coefficients of the linear fitting. Hence, the lateral-referenced OCT signal can be found as

$$\widetilde{I}^{Tref}_{lateral}(x,z,t) = \widetilde{I}^{Tref}(x,z,t)\exp\left[-j\phi^{fit}(x,t)\right] \tag{18}$$

where j is the imaginary unit. We applied a Gaussian filter (kernel size: 5×7 pixels) on the complex-valued signal to enhance the SNR and then extract lateral-referenced phase signals,

$$\phi^{Tref}_{lateral}(x,z,t) = \measuredangle\left[\widetilde{I}^{Tref}_{lateral}(x,z,t) \circledast G(x,z)\right] \tag{19}$$

where G is the Gaussian kernel and $\circledast$ denotes the convolution operation. Finally, the laterally referenced ΔOPL can be computed as

$$\Delta\mathrm{OPL}^{(\exp)} = \phi^{Tref}_{lateral}(x,z,t)\frac{\lambda_c}{4\pi} \tag{20}$$

where $\lambda_c = 840$ nm denotes the central wavelength of the OCT imaging beam.

Model-derived ΔOPL computation

For the axisymmetric model, we denote the lateral dimension as r. The variables of interest for ΔOPL computation from the model are $u_z(r,z,t)$ and $\Theta(r,z,t)$. For simplicity, we assume that the refractive index of the retinal tissue follows the same temperature dependence as of water. Hence, the single-pass OPL change at any point in space and time can be approximated as

$$\Delta\mathrm{OPL}(r,z,t) \approx n_{\mathrm{RT}} \cdot u_z(r,z,t) + \int_{z_0}^{z} \alpha_{\mathrm{TO}}\Theta(r,z,t)dz \tag{21}$$

where n_{RT} is the refractive index of tissue at room temperature, and α_{TO} is the thermo-optic coefficient. Within the temperature range of interest, 37–60 °C, the temperature dependence of $n_{\mathrm{water}}(\Theta)$ varies between -1.4×10^{-4} and -1.8×10^{-4} K^{-1} [42]. For simplicity, a linear variation with a slop of $\alpha_{\mathrm{TO}} = -1.6\times10^{-4}$ K^{-1} was used in this work. The refractive index at ambient temperature was taken to be 1.37[52]. As in the experimental data processing, the model-derived OPL changes were laterally referenced to the boundaries of the OCT B-scan.

Acknowledgements
We thank Dr. Bingyao Tan for fruitful discussions of the optical setup. This work was funded by the National Institutes of Health (U01 EY032055), Air Force Office of Scientific Research (FA9550-20-1-0186) and Research to Prevent Blindness.

Author details
[1]Department of Electrical Engineering, Stanford University, Stanford, CA 94305, USA. [2]Hansen Experimental Physics Laboratory, Stanford University, Stanford, CA 94305, USA. [3]Department of Ophthalmology, Stanford University, Stanford, CA 94305, USA. [4]School of Chemistry, Chemical Engineering and Biotechnology, Nanyang Technological University, Singapore, Singapore. [5]Department of Mechanical Engineering, The University of Tokyo, Tokyo, Japan. [6]Wellman Center for Photomedicine, Harvard Medical School, Massachusetts General Hospital, Boston, MA 02114, USA. [7]Singapore Eye Research Institute, Singapore National Eye Centre, Singapore, Singapore. [8]SERI-NTU Advanced Ocular Engineering (STANCE) Program, Singapore, Singapore. [9]School of Electrical and Electronic Engineering, Nanyang Technological University, Singapore, Singapore

Author contributions
Y.Z., D.V., and D.P. designed research; Y.Z. and J.H. built the optical setup; Y.Z., M.B., and D.P.H. performed experiments; H.L. and T.L. developed the subpixel motion correction algorithm; Y.Z. and H.L. processed the experimental data; Y.Z. and D.V. performed computational modeling; Y.Z., H.L., M.B., and D.P. wrote the paper.

Data availability
The data supporting the findings of this study are available from the corresponding author upon reasonable request.

Conflict of interest
The authors declare no competing interests.

Supplementary information The online version contains supplementary material available at https://doi.org/10.1038/s41377-025-01798-x.

Received: 30 August 2024 Revised: 16 February 2025 Accepted: 18 February 2025
Published online: 02 April 2025

References

1. Paulus, Y. M. et al. Selective retinal therapy with microsecond exposures using a continuous line scanning laser. *Retina* **31**, 380–388 (2011).
2. Roider, J. et al. Microphotocoagulation: selective effects of repetitive short laser pulses. *Proc. Natl. Acad. Sci. USA* **90**, 8643–8647 (1993).
3. Sramek, C. et al. Dynamics of retinal photocoagulation and rupture. *J. Biomed. Opt.* **14**, 034007 (2009).
4. Schmidt, S. Y. & Peisch, R. D. Melanin concentration in normal human retinal pigment epithelium. Regional variation and age-related reduction. *Investig. Ophthalmol. Vis. Sci.* **27**, 1063–1067 (1986).
5. Dillon, J. et al. Transmission of light to the aging human retina: possible implications for age related macular degeneration. *Exp. Eye Res.* **79**, 753–759 (2004).
6. Kessel, L. et al. Age-related changes in the transmission properties of the human lens and their relevance to circadian entrainment. *J. Cataract Refract. Surg.* **36**, 308–312 (2010).
7. Simanovskii, D. M. et al. Cellular tolerance to pulsed hyperthermia. *Phys. Rev. E* **74**, 011915 (2006).
8. Sramek, C. et al. Non-damaging retinal phototherapy: dynamic range of heat shock protein expression. *Investig. Ophthalmol. Vis. Sci.* **52**, 1780–1787 (2011).
9. Lavinsky, D. & Palanker, D. Nondamaging photothermal therapy for the retina: initial clinical experience with chronic central serous retinopathy. *Retina* **35**, 213–222 (2015).
10. Lavinsky, D. et al. Nondamaging retinal laser therapy: rationale and applications to the macula. *Investig. Ophthalmol. Vis. Sci.* **57**, 2488–2500 (2016).
11. Luttrull, J. K. & Dorin, G. Subthreshold diode micropulse laser photocoagulation (SDM) as invisible retinal phototherapy for diabetic macular edema: a review. *Curr. Diab. Rev.* **8**, 274–284 (2012).
12. Mordmüller, M. et al. Towards temperature controlled retinal laser treatment with a single laser at 10 kHz repetition rate. *Adv. Opt. Technol.* **10**, 423–431 (2021).
13. Vakoc, B. J., Tearney, G. J. & Bouma, B. E. Real-time microscopic visualization of tissue response to laser thermal therapy. *J. Biomed. Opt.* **12**, 020501 (2007).
14. Kurokawa, K. et al. Two-dimensional micro-displacement measurement for laser coagulation using optical coherence tomography. *Biomed. Opt. Express* **6**, 170–190 (2015).
15. Makita, S. & Yasuno, Y. In vivo photothermal optical coherence tomography for non-invasive imaging of endogenous absorption agents. *Biomed. Opt. Express* **6**, 1707–1725 (2015).
16. Muqit, M. M. K. et al. Study of clinical applications and safety for Pascal® laser photocoagulation in retinal vascular disorders. *Acta Ophthalmol.* **90**, 155–161 (2012).
17. Amoroso, F. et al. OCTA-guided navigated laser therapy for advanced macula neovascularization secondary to age related macular degeneration. *Eur. J. Ophthalmol.* **31**, 3182–3189 (2021).
18. Müller, H. H. et al. Imaging thermal expansion and retinal tissue changes during photocoagulation by high speed OCT. *Biomed. Opt. Express* **3**, 1025–1046 (2012).
19. Salimi, M. H., Villiger, M. & Tabatabaei, N. Transient-mode photothermal optical coherence tomography. *Opt. Lett.* **46**, 5703–5706 (2021).
20. Veysset, D. et al. Interferometric thermometry of ocular tissues for retinal laser therapy. *Biomed. Opt. Express* **14**, 37–53 (2023).
21. Veysset, D. et al. Interferometric imaging of thermal expansion for temperature control in retinal laser therapy. *Biomed. Opt. Express* **13**, 728–743 (2022).
22. Pandiyan, V. P. et al. The optoretinogram reveals the primary steps of phototransduction in the living human eye. *Sci. Adv.* **6**, eabc1124 (2020).
23. Gullapalli, V. K. et al. Transplantation frontiers. in *Retina* 2058–2077 (Elsevier, 2013).
24. Lee, K. E., Heitkotter, H. & Carroll, J. Challenges associated with ellipsoid zone intensity measurements using optical coherence tomography. *Transl. Vis. Sci. Technol.* **10**, 27 (2021).
25. Cai, C. X. et al. A comparison of progressive loss of the ellipsoid zone (EZ) band in autosomal dominant and x-linked retinitis pigmentosa. *Investig. Ophthalmol. Vis. Sci.* **55**, 7417–7422 (2014).
26. Jonnal, R. S. et al. The cellular origins of the outer retinal bands in optical coherence tomography images. *Investig. Ophthalmol. Vis. Sci.* **55**, 7904–7918 (2014).
27. Wensel, T. G. et al. Structure and dynamics of photoreceptor sensory cilia. *Pflüg. Arch. Eur. J. Physiol.* **473**, 1517–1537 (2021).
28. Tan, B. Y. et al. Light-evoked deformations in rod photoreceptors, pigment epithelium and subretinal space revealed by prolonged and multilayered optoretinography. *Nat. Commun.* **15**, 5156 (2024).
29. Li, H. K. et al. Phase-restoring subpixel image registration: enhancing motion detection performance in Fourier-domain optical coherence tomography. *J. Phys. D Appl. Phys.* **58**, 145102 (2025).
30. Bahar, L. Y. Transfer matrix approach to layered systems. *J. Eng. Mech. Div.* **98**, 1159–1172 (1972).
31. Yue, Z. Q. & Yin, J. H. Backward transfer-matrix method for elastic analysis of layered solids with imperfect bonding. *J. Elast.* **50**, 109–128 (1998).
32. Wang, L. & Rokhlin, S. I. Stable reformulation of transfer matrix method for wave propagation in layered anisotropic media. *Ultrasonics* **39**, 413–424 (2001).
33. Ai, Z. Y., Cheng, Z. Y. & Han, J. State space solution to three-dimensional consolidation of multi-layered soils. *Int. J. Eng. Sci.* **46**, 486–498 (2008).
34. Candiello, J., Cole, G. J. & Halfter, W. Age-dependent changes in the structure, composition and biophysical properties of a human basement membrane. *Matrix Biol.* **29**, 402–410 (2010).
35. Vielmuth, F. et al. Biomechanical properties of the internal limiting membrane after intravitreal ocriplasmin treatment. *Ophthalmologica* **235**, 233–240 (2016).
36. Kennedy, B. F. et al. Optical coherence micro-elastography: mechanical-contrast imaging of tissue microstructure. *Biomed. Opt. Express* **5**, 2113–2124 (2014).
37. Qu, Y. Q. et al. Quantified elasticity mapping of retinal layers using synchronized acoustic radiation force optical coherence elastography. *Biomed. Opt. Express* **9**, 4054–4063 (2018).
38. Qu, Y. Q. et al. In vivo elasticity mapping of posterior ocular layers using acoustic radiation force optical coherence elastography. *Investig. Ophthalmol. Vis. Sci.* **59**, 455–461 (2018).
39. Khanna, H. Photoreceptor sensory cilium: traversing the ciliary gate. *Cells* **4**, 674–686 (2015).
40. Rosenbluth, M. J., Lam, W. A. & Fletcher, D. A. Force microscopy of non-adherent cells: a comparison of leukemia cell deformability. *Biophys. J.* **90**, 2994–3003 (2006).
41. Spedden, E. et al. Elasticity maps of living neurons measured by combined fluorescence and atomic force microscopy. *Biophys. J.* **103**, 868–877 (2012).
42. Goetz, G. et al. Interferometric mapping of material properties using thermal perturbation. *Proc. Natl. Acad. Sci. USA* **115**, E2499–E2508 (2018).
43. Lozano, D. C. & Twa, M. D. Development of a rat schematic eye from in vivo biometry and the correction of lateral magnification in SD-OCT imaging. *Investig. Ophthalmol. Vis. Sci.* **54**, 6446–6455 (2013).
44. Gao, F. C. & Han, L. X. Implementing the Nelder-Mead simplex algorithm with adaptive parameters. *Comput. Optim. Appl.* **51**, 259–277 (2012).
45. Efron, B. Bootstrap methods: another look at the jackknife. *Ann. Stat.* **7**, 1–26 (1979).
46. Efron, B. & Tibshirani, R. Improvements on cross-validation: the 632+ bootstrap method. *J. Am. Stat. Assoc.* **92**, 548–560 (1997).
47. Stefánsson, E. et al. Panretinal photocoagulation and retinal oxygenation in normal and diabetic cats. *Am. J. Ophthalmol.* **101**, 657–664 (1986).
48. Lavinsky, D. et al. Functional and structural effects of nondamaging retinal laser therapy for macular telangiectasia type 2: a randomized sham-controlled clinical trial. *Retina* **41**, 487–494 (2021).
49. Seifert, E. et al. Selective retina therapy: toward an optically controlled automatic dosing. *J. Biomed. Opt.* **23**, 115002 (2018).
50. Latina, M. A. et al. Q-switched 532-nm Nd:YAG laser trabeculoplasty (selective laser trabeculoplasty). *Ophthalmology* **105**, 2082–2090 (1998).
51. Guizar-Sicairos, M., Thurman, S. T. & Fienup, J. R. Efficient subpixel image registration algorithms. *Opt. Lett.* **33**, 156–158 (2008).
52. Chen, E. P. Refractive indices of the rat retinal layers. *Acta Ophthalmol.* **71**, 1e–9e (1993).